Rich Falcon

Nanocrystals

Processes, Properties and Applications

Nanocrystals: Processes, Properties and Applications

Edited by **Rich Falcon**

NY RESEARCH PRESS
New York

Published by NY Research Press,
23 West, 55th Street, Suite 816,
New York, NY 10019, USA
www.nyresearchpress.com

Nanocrystals: Processes, Properties and Applications
Edited by Rich Falcon

International Standard Book Number: 978-1-63238-335-8 (Hardback)

Printed in China.

Nanocrystals: Processes, Properties and Applications

Preface

This book aims to highlight the current researches and provides a platform to further the scope of innovations in this area. This book is a product of the combined efforts of many researchers and scientists, after going through thorough studies and analysis from different parts of the world. The objective of this book is to provide the readers with the latest information of the field.

Nanocrystals research has been crucial due to the wide range of potential functions in semiconductor, visual and biomedical fields. This book compiles work on nanocrystals processing, and classification of their structural, visual, electronic, magnetic and mechanical properties. A variety of methods for nanocrystals synthesis is presented in this book. Nanocrystals when combined with several other materials systems have shown enhanced properties. An appraisal of the outcomes that nanoparticles research has provided indicates additional accomplishments in the near future.

I would like to express my sincere thanks to the authors for their dedicated efforts in the completion of this book. I acknowledge the efforts of the publisher for providing constant support. Lastly, I would like to thank my family for their support in all academic endeavors.

Editor

Contents

Chapter 1

Carrier Dynamics and Magneto-Optical Properties of $Cd_{1-x}Mn_xS$ Nanoparticles

Noelio Oliveira Dantas and Ernesto Soares de Freitas Neto

Additional information is available at the end of the chapter

1. Introduction

$Cd_{1-x}Mn_xS$ nanoparticles (NPs) with size quantum confinement belong to the diluted magnetic semiconductor (DMS) quantum dot (QD) class of materials that has been widely studied in the last few years. The study of quasi-zero-dimensional Diluted Magnetic Semiconductors (DMS), such as $Cd_{1-x}Mn_xS$ Quantum Dots (QDs), is strongly motivated due to the localization of magnetic ions in the same places as the free-like electron and hole carriers occurring in these nanomaterials **[1,2]**. This interesting phenomenon causes unique properties in DMS dots that can be explored in different technological applications, such as wavelength tunable lasers**[3]**, solar cells**[4,5]**, or in spintronic devices**[6,7]**. In this context, glass matrix-encapsulated $Cd_{1-x}Mn_xS$ NPs emerge as potential candidates for several applications, given that this host transparent material is robust and provides excellent stability for DMS nanostructures. Therefore, the luminescent properties and carrier dynamics of $Cd_{1-x}Mn_xS$ NPs should be comprehensively understood in order to target optical applications. For instance, different models based on rate equations can be employed to describe the temperature-dependent carrier dynamics of DMS nanostructures, such as they have been applied to semiconductor quantum wells**[8]**, N-impurity complexes in III–V materials**[9]**, and self-assembled semiconductor quantum dots**[10]**.

It is well known that the optical properties of NPs can be significantly changed by interactions between nanostructures and their host material, due mainly to the formation of surface defects **[11, 12]**. These surface defects are heavily dependent on NP size and become more important with increasing surface–volume ratio. Generally, the comparison between the optical properties of $Cd_{1-x}Mn_xS$ QDs and their corresponding bulk is obtained in different environments. To the best of our knowledge, this study is probably the first that simultaneously investigates both the carrier dynamics and the magneto-optical properties of $Cd_{1-x}Mn_xS$ QDs and their corresponding bulk-like NC when both are embedded in the same host material.

Although the dot doped with impurities (metal and magnetic) are currently being synthesized by colloidal chemistry techniques **[13,14]**, some possible applications require the nanoparticles (NPs) being embedded in robust and transparent host materials. In this context, the melting-nucleation approach appears as an appropriate synthesis technique since it allows the growth of DMS nanocrystals (NCs) embedded in different glass matrices. In addition to the controllable dot size and Mn^{2+} ion fraction incorporated into $Cd_{1-x}Mn_xS$ dots which can be achieved by this synthesis protocol, for example, the host glass matrix provides an excellent stability to the NPs. In particular for the melting-nucleation protocol used in this chapter, it is presented a discussion on the doping of QDs with magnetic impurities reasoned in two main models**[3]**: the 'trapped-dopant' and 'self-purification' mechanisms.

In this chapter, we have employed the optical absorption (OA), magnetic force microscopy (MFM), photoluminescence (PL), and magnetic circularly polarized photoluminescence (MCPL) measurements in order to investigate the properties of $Cd_{1-x}Mn_xS$ NPs that were successfully grown in a glass matrix. The organization of this chapter is shown as follows. In the section 2 (next section), we present the synthesis protocol that was employed in order to grow $Cd_{1-x}Mn_xS$ NPs in a glass matrix. The results obtained from the experimental techniques are presented and discussed in the section 3, highlighting the carrier dynamics and the magneto-optical properties of nanoparticles. We conclude our study in the section 4.

2. Synthesis of $Cd_{1-x}Mn_xS$ nanoparticles in a glass matrix

The host glass matrix for NP growth was labeled SNAB since its nominal composition is: $40SiO_2.30Na_2CO_3.1Al_2O_3.29B_2O_3$ (mol %). $Cd_{1-x}Mn_xS$ NPs were successfully synthesized in this glass matrix by adding 2[CdO + S] (wt % of SNAB), and x[Mn] (wt % of Cd), with x = 0.0, 0.5, 5.0, and 10 %. The synthesis method consists in a two sequential melting-nucleation approach, in which it is possible obtain ensembles of nearly spherical nanoparticles embedded in a glass matrix **[12]**. First, the powder mixture was melted in an alumina crucible at 1200 ºC for 30 minutes. Next, the melted mixture was quickly cooled down to room temperature where diffusion of Cd^{2+}, Mn^{2+}, and S^{2-} species took place. This diffusion resulted in $Cd_{1-x}Mn_xS$ NP growth in the SNAB glass environment.

In a second stage, a sample with x = 0.100 was subjected to a thermal annealing at 560 ºC for 6 h in order to enhance the diffusion of ions within the host SNAB matrix which promotes the growth of magnetic dots. Room temperature XRD pattern of the undoped CdS NPs (x = 0) embedded in the SNAB glass matrix was recorded with a XRD-6000 Shimadzu diffractometer using monochromatic Cu-$K_{\alpha 1}$ radiation (λ = 1.54056 Å). Thus, the wurtzite structure of CdS NPs embedded in the SNAB glass matrix has been confirmed. Evidently, the $Cd_{1-x}Mn_xS$ NPs with diluted magnetic doping have this same wurtzite structure, since it is a common phase for this DMS material.

3. Results and discussions

We have employed several experimental techniques in order to investigate the carrier dynamics and the magneto-optical properties of $Cd_{1-x}Mn_xS$ NPs. The room temperature

absorption band edge of synthesized $Cd_{1-x}Mn_xS$ NCs was obtained with a double beam UV – VIS – NIR spectrophotometer (Varian, Cary 500) operating between 250 and 800 nm and with a spectral resolution of 1 nm. Photoluminescence (PL) measurements were taken with a 405 nm (~3.06 eV) continuous wave laser focused on a ~200 μm ray spot with an excitation power of 2.5 mW. $Cd_{1-x}Mn_xS$ NP luminescence was collected using a USB4000 spectrometer from Ocean Optics equipped with a Toshiba TCD1304AP 3648-element linear CCD-array detector, in the 10 K to 300 K temperature range, with a 435 nm high-pass filter. The magnetic force microscopy images of the $Cd_{1-x}Mn_xS$ NPs doped with x = 0.100 were recorded at room temperature with a scanning probe microscope (Shimadzu, SPM – 9600).

The magneto-photoluminescence (MPL) measurements were performed using superconductor coils (Oxford Instruments) with fields up to 15 T. The samples were placed into the liquid helium cryostat at 2 K and excited using a 405 nm (± 5 nm) continuous wave laser, from Laserline Laser Technology, focused on ~ 200 μm rays spot with excitation intensity values of 10 mW. The detected MPL was carried out with an ocean optics spectrometer (USB4000) and the polarization was analyzed using a $\lambda/4$ waveplate and with linear polarizer fixed parallel to the spectrometer entrance, in order to collect the photons with σ^+ and σ^- circular polarizations, respectively.

3.1. Carrier dynamics

The room temperature OA spectra of $Cd_{1-x}Mn_xS$ NPs, with different x-concentrations, are shown in Fig. 1a. The formation of two well defined groups of $Cd_{1-x}Mn_xS$ NPs of different sizes was confirmed by the two bands in the OA spectra. As indicated in Fig. 1a, these two groups of NPs were named: (i) QDs because their quantum confinement properties provoked a change in band energy around ~3 eV; and (ii) bulk-like NCs indicated by the absence of quantum confinement given the fixed band around ~2.58 eV, a value near the energy gap of bulk CdS **[15,16]**. At the bottom of Fig. 1a is the OA spectrum of the SNAB glass matrix where, in contrast, it can be seen that over a broad spectral range there is a complete absence of any band associated with NPs.

Figure 1a shows that the undoped CdS QDs (x = 0.000) exhibit confinement energy (E_{conf}) as indicated by the OA band peak at ~3.10 eV. From this value and using a confinement model based on effective mass approximation**[12,15-18]**, the mean QD radius R was estimated by the expression: $E_{conf} = E_g + (\hbar^2\pi^2 / 2\mu R^2) - 1.8(e^2 / \varepsilon R)$, where E_g is the bulk material energy gap, μ is the reduced effective mass, e is the elementary charge, and ε is the dielectric constant. From this, a mean radius of about R~2.0 nm was estimated for the CdS QDs, thus confirming strong size quantum confinement **[16]**.

Furthermore, the increase in x-concentration clearly induced a blue shift in the OA band of the $Cd_{1-x}Mn_xS$ QDs from ~3.10 eV (x = 0.000) to ~3.22 eV for the highest magnetic doping (x = 0.100). Since these QDs were grown under identical synthesis conditions within the glass environment, it is expected that they would have the same mean size. As a result, there were no significant differences in the quantum confinements of these QDs that would cause shifts in the OA band peaks. Thus, it was concluded that the observed blue shift in OA band peak

(Fig. 1a) was a consequence of the **sp-d** exchange interactions between electrons confined in dot states and those located in the partially filled Mn^{2+} states. This explanation is reasonable since replacing Cd^{2+} with Mn^{2+} ions should increase the energy gap of $Cd_{1-x}Mn_xS$ QDs**[18]**. In addition, it is interesting to note the weak **sp-d** exchange interaction in the $Cd_{1-x}Mn_xS$ bulk-like NCs because their OA band remains in an almost fixed position (~2.58 eV).

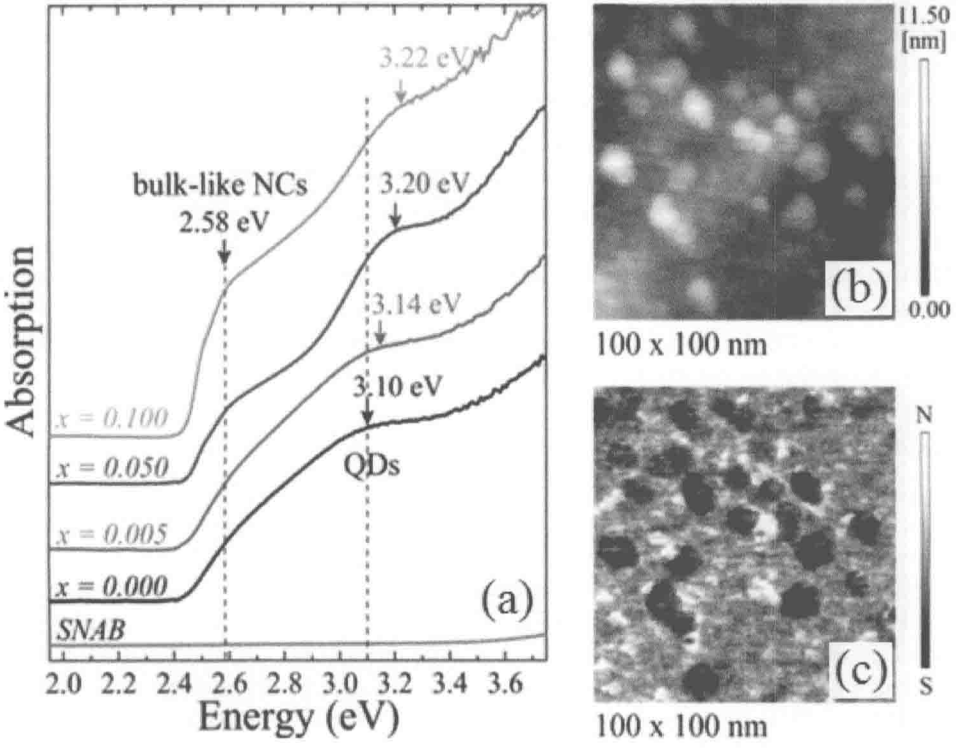

Figure 1. (a) Room temperature OA spectra of $Cd_{1-x}Mn_xS$ NPs with different x-concentrations embedded in the SNAB glass matrix. The two groups of NPs (QDs and bulk-like NCs) are indicated by the vertical dashed lines. The OA spectrum of the SNAB glass matrix is also shown at the bottom for comparison. (b) Topographic MFM image showing high quantities of $Cd_{0.900}Mn_{0.100}S$ NPs at the sample's surface, and (c) the corresponding phase MFM image (30 nm lift) where the contrast between the North (N) and South (S) magnetic poles identifies the orientation of the total magnetic moment of the DMS NPs.

Figure 1b presents the two-dimensional (100 x 100 nm) topographic MFM image of the sample with the highest level of magnetic doping (x = 0.100). Like the OA spectra, the topographic MFM image confirms the formation of two well defined groups of NPs with different mean radii: (i) R ~ 2.1 nm for the QDs, which closely agrees with the result estimated from the OA data (R ~ 2.0 nm); and (ii) R ~ 10.0 nm for the bulk-like NCs, a value near the vertical scale edge of Fig. 1b. Evidently, the exciton Bohr radius of bulk $Cd_{1-x}Mn_xS$ with diluted magnetic doping should be near that of bulk CdS, which is around a_B ~ 3.1 nm **[16]**. Hence, we can conclude that the QDs with mean radius R ~ 2.0 nm are under strong

quantum confinement, while the bulk-like NCs with mean radius R ~ 10.0 nm hardly exhibit any size confinement**[19]**.

In addition, a large quantity $Cd_{1-x}Mn_xS$ NPs can be observed in Fig. 1b, as well as in the corresponding phase MFM image shown in Fig. 1c. These images reveal great proximity between the two groups of NPs (QDs and bulk-like NCs), so that strong coupling between their wave functions is expected. In Fig. 1c, the topographic signal can be neglected because its phase MFM was recorded with a 30 nm lift from the sample's surface. Thus, interaction between tip and NP magnetization induces the contrast observed in this phase MFM image. The dark area (light area) is caused by attraction (repulsion) between tip and NP magnetization represented by the South (North) magnetic pole in the vertical scale bar of Fig. 1c. Evidently, the magnetization in each NP (QD or bulk-like NC) is caused by the size-dependent **sp-d** exchange interactions, proving that Mn^{2+} ions are incorporated into the DMS nanostructures. This Mn^{2+} ion incorporation in NPs has also been established by electron paramagnetic resonance (EPR) measurements and simulations with other samples synthesized in the same way as in this research **[17]**. In Fig. 1c, it is interesting to note that there is a relationship between the NP size and the direction of its magnetic moment: small (large) NPs have their magnetic moment oriented towards the North (South) pole.

Figures 2a and b present, as examples, the effect of temperature on $Cd_{1-x}Mn_xS$ NP luminescence with x = 0.000 and 0.050. The emissions from the two groups of $Cd_{0.950}Mn_{0.050}S$ NPs with different sizes, QDs and bulk-like NCs, are clearly identified in Fig. 2b by the presence of two well defined PL bands which are in agreement with the OA spectra of Fig. 1. However, in Fig. 2a, a PL band can be observed whose complex nature is a result of the overlapping of several emissions, including those from deep defects: denominated as (1) and (2) for the QDs, as well as $(1)^b$ and $(2)^b$ for the bulk-like NCs. In a recent study of other similar $Cd_{1-x}Mn_xS$ NPs with wurtzite structure, the existence of emissions from two trap levels related to the presence of deep defects was demonstrated**[20]**. The origin of these defects in $Cd_{1-x}Mn_xS$ NPs (and CdS NPs) with hexagonal wurtzite structure is possibly related to two energetically different $V_{Cd} - V_S$ divacancies: one oriented along the hexagonal c-axis (assigned to trap (1)), and the other oriented along the basal Cd-S bond (assigned to trap (2))**[20]**. Furthermore, the size-dependence of these trap-levels, (1) and (2), has been confirmed for CdSe NCs **[21]**, explaining the observed emissions from them in both the QDs (E_1 and E_2) and bulk-like NCs (E_1^b and E_2^b) that are embedded in our glass samples.

In Figs. 2a and b, all emissions are marked by vertical dotted lines, including the bound exciton emission (E_{exc}) of QDs as well as the electron-hole recombination (E_b) of bulk-like NCs. The characteristic emission of Mn^{2+} ions (E_{Mn}~2.12 eV) between the $^4T_1 - {}^6A_1$ levels in the $Cd_{1-x}Mn_xS$ NPs (with $x \neq 0$) is also evident and represented in the Fig. 2c by $1/\tau_r^{Mn}$ rate **[1,22,23]**. The complete recombination aspects of these PL spectra are well-described in a diagram in Fig. 2c, where six (seven) emission bands can be identified for the CdS NPs ($Cd_{1-x}Mn_xS$ NPs with $x \neq 0$). In Fig. 2b, the asymmetric shape of the emission band around 480 nm at low temperatures confirms the presence of shallow virtual levels for the QDs, and evidently there is also for the bulk-like NCs, as depicted in Fig. 2c. However, this emission

band (480 nm) becomes symmetric with rising temperature, which demonstrates that the trapped carriers in the virtual levels are being released to other non-radiative channels of QDs. It is interesting to note that in Fig. 2a the excitonic emission (E_{exc}) of CdS QDs is almost suppressed due to the strong presence of non-radiative channels, including one related to the energy transfer from QDs to bulk-like NCs. However, a comparison between the PL spectra of the CdS and the $Cd_{0.950}Mn_{0.050}S$ NPs (see Fig. 2) clearly reveals that increasing x-concentration induces gradual suppression of emissions from all trap-levels ((1), (2), $(1)^b$, and $(2)^b$), since Mn^{2+} ions are replacing the V_{Cd} vacancies in the NPs. Indeed, this fascinating behavior provides further evidence that the deep defects are caused by V_{Cd} –V_S divacancies, and that the NPs are actually being doped by Mn^{2+} ions. Hence, the non-radiative channels that supply the deep trap-levels disappear with increasing x-concentration in $Cd_{0.950}Mn_{0.050}S$ NPs, as shown in Fig. 2b.

In Fig. 2c, the wavy arrows represent non-radiative channels from the excitonic states of QDs, and from the conduction band (CB) of bulk-like NCs. Here, non-radiative energy transfer (ET) is given by the rate $1/\tau_{ET}^{n}$ (with n = A, B, C, A', and B'), where τ_{ET}^{n} is the carrier escape time from an NP to one of these five non-radiative transitions. In our model, we have assumed that the non-radiative paths from the excitonic states of QDs, as well as from the conduction band of bulk-like NCs to the deep trap-levels ((1), (2), $(1)^b$, and $(2)^b$) can be disregarded. However, it is evident that these deep trap-levels may be filled by carriers from: (i) the shallow virtual levels of QDs and bulk-like NCs; and (ii) the $^4T_1$ levels of Mn^{2+} ions**[20]**. Energy transfers from the excitonic states of QDs follow three paths: (A) to virtual levels (QDs); (B) to the conduction band of bulk-like NCs; and (C) to the $^4T_1$ level of Mn^{2+} ions. On the other hand, the energy transfers from the conduction band of bulk-like NCs follow two paths: (A') to virtual levels (bulk); and (B') to the $^4T_1$ level of Mn^{2+} ions. It is well known that the very fast energy transfer from a NP to Mn^{2+} ions is generally resonant due to the high density of states above the emissive $^4T_1$ level,[1] as shown by the $^{2,4}\Gamma$ levels in Fig. 2c. However, size quantum confinement can play an important role in this process that, besides being mediated by the **sp-d** exchange interactions, is strongly dependent on the Mn^{2+} fraction in $Cd_{1-x}Mn_xS$ NPs. In other words, QDs and bulk-like NCs are expected to behave differently due to the strong confinement of the QDs with a small mean radius of about R~2.0 nm.

The excitonic states of QDs can be denoted by $|1\rangle$, and the CB of bulk-like NCs by $|1^b\rangle$. The carrier number (depending on temperature T) of these two states is given by $N_1(T)$ and $N_1^b(T)$, respectively. Since carriers are thermally distributed each one of the three non-radiative channels related to QDs is supplied by $N_1(T)\exp(-E_n/K_BT)$ carriers, where E_n (with n = A, B, and C) is the corresponding activation energy of the non-radiative n channel. Similarly, $N_1^b(T)\exp(-E_n/K_BT)$ carriers are transferred to each one of the two non-radiative channels related to bulk-like NCs, where n = A', and B'. Furthermore, as shown in Fig. 2c by the straight, downward pointing arrows, radiative emissions are also present from both QDs and bulk-like NCs in the PL spectra which are related to $1/\tau_r^{QD}$ and $1/\tau_r^{b}$ rates, respectively. The straight, upward pointing arrow, indicated by g (g'), represents photo-excitation of the QDs (bulk-like NCs) caused by the laser pump. The carrier dynamics that take into account

these transitions from the $|1\rangle$ (QD) and $|1^b\rangle$ (bulk-like NC) levels can be described by the following rate equations:

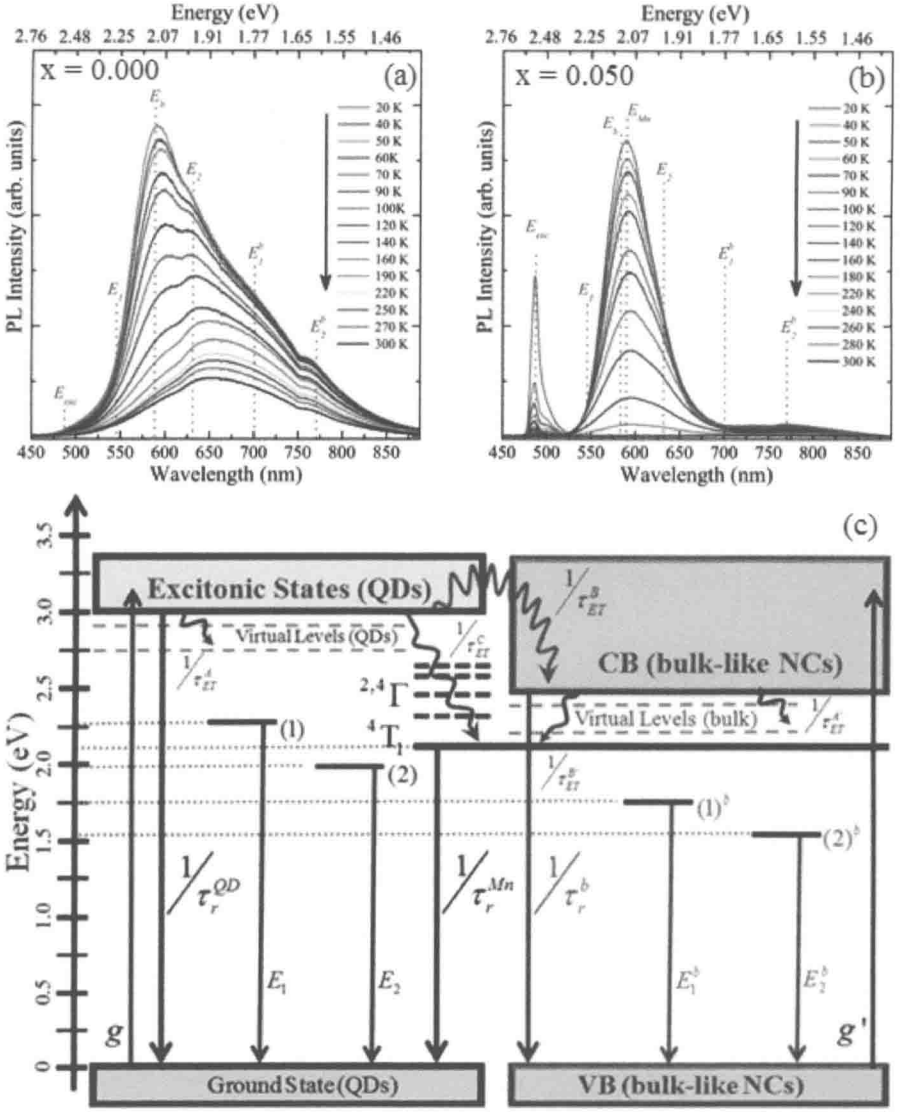

Figure 2. PL spectra of both (a) the CdS NPs (x = 0.000) and (b) $Cd_{0.950}Mn_{0.050}S$ NPs at several temperatures, from 20 K (top) to 300 K (bottom), as indicated by the downward pointing arrows. Their recombination aspects are depicted in panel (c), where the emissions from both the QDs and the bulk-like NCs are clearly identified. In addition, the characteristic emission of Mn^{2+} ions ($^4T_1$–$^6A_1$), E_{Mn} ~2.12 eV, when substitutionally incorporated in II-VI semiconductors is also evident. In the present energy scale, the $^6A_1$ level of the Mn^{2+} ions is located at top of the QD ground state.

$$\frac{dN_1(T)}{dt} = +g - \underbrace{\frac{N_1(T)}{\tau_r^{QD}}}_{\text{radiative emission}} - \underbrace{\frac{N_1(T)\beta_A}{\tau_{ET}^{A}}}_{\text{QDs}\rightarrow\text{virtual levels (QDs)}} - \underbrace{\frac{N_1(T)\beta_B}{\tau_{ET}^{B}}}_{\text{QDs}\rightarrow\text{bulk-like NCs}} - \underbrace{\frac{N_1(T)\beta_C}{\tau_{ET}^{C}}}_{\text{QDs}\rightarrow Mn^{2+}\text{ ions}} ; \quad (1)$$

$$\frac{dN_1^b(T)}{dt} = +g' + \underbrace{\frac{N_1(T)\beta_B}{\tau_{ET}^{B}}}_{\text{QDs}\rightarrow\text{bulk-like NCs}} - \underbrace{\frac{N_1^b(T)}{\tau_r^{b}}}_{\text{radiative emission}} - \underbrace{\frac{N_1^b(T)\beta_{A'}}{\tau_{ET}^{A'}}}_{\text{bulk-like NCs}\rightarrow\text{virtual levels (bulk)}} - \underbrace{\frac{N_1^b(T)\beta_{B'}}{\tau_{ET}^{B'}}}_{\text{bulk-like NCs}\rightarrow Mn^{2+}\text{ ions}} ; \quad (2)$$

where $\beta_n = \exp\left(-E_n/K_BT\right)$ with n = A, B, C, A′, and B′. In Eqs. (1) and (2), both the radiative emissions from QDs and bulk-like NCs and all non-radiative energy transfers are highlighted. In steady-state conditions, the laser excitations are given by $g = N_{1(0)}/\tau_r^{QD}$ and $g' = N_{1(0)}^b/\tau_r^b$ for QDs and bulk-like NCs, respectively. Moreover, there are no temporal changes in the carrier numbers, i.e., $\left(dN_1(T)/dt\right) = 0$ and $\left(dN_1^b(T)/dt\right) = 0$. When these conditions are replaced in Eqs. (1) and (2), we get:

$$N_1(T) = \frac{N_{1(0)}}{\left[1 + \alpha_A \exp\left(\frac{-E_A}{K_BT}\right) + \alpha_B \exp\left(\frac{-E_B}{K_BT}\right) + \alpha_C \exp\left(\frac{-E_C}{K_BT}\right)\right]} ; \quad (3)$$

$$0 = +\frac{N_{1(0)}^b}{\tau_r^b} + N_1(T)\frac{\exp\left(\frac{-E_B}{K_BT}\right)}{\tau_{ET}^{B}} - N_1^b(T)\left[\frac{1}{\tau_r^b} + \frac{\exp\left(\frac{-E_{A'}}{K_BT}\right)}{\tau_{ET}^{A'}} + \frac{\exp\left(\frac{-E_{B'}}{K_BT}\right)}{\tau_{ET}^{B'}}\right] . \quad (4)$$

The carriers' number in the QDs ($|1\rangle$ level) as a function of temperature T is given by Eq. (3), where the term $\alpha_n = \left(\tau_r^{QD}/\tau_{ET}^{n}\right)$ (with n = A, B, and C) can be considered constant at first approximation. After replacing the term $N_1(T)$ (given by Eq. (3)) in Eq. (4), we get:

$$0 = +\frac{N_{1(0)}^b}{\tau_r^b} + \frac{N_{1(0)}}{\tau_{ET}^{B}\left[\exp\left(\frac{E_B}{K_BT}\right) + \alpha_A \exp\left[\frac{-\left(E_A - E_B\right)}{K_BT}\right] + \alpha_B + \alpha_C \exp\left[\frac{-\left(E_C - E_B\right)}{K_BT}\right]\right]} - N_1^b(T)\left[\frac{1}{\tau_r^b} + \frac{\exp\left(\frac{-E_{A'}}{K_BT}\right)}{\tau_{ET}^{A'}} + \frac{\exp\left(\frac{-E_{B'}}{K_BT}\right)}{\tau_{ET}^{B'}}\right] . \quad (5)$$

Evidently, the second term on the right side of Eq. (5) is related to the carrier-mediated energy transfer from QDs to bulk-like NCs, and can be defined by: